

From Bloch to Néel: Anisotropy-dependent Domain-Wall Character in FePd Thin Films

Annika Stellan,^{1,*} Alicia Backs,¹ Ekaterina Klyushina,² Connie Bednarski-Meinke,³ Steffen Tober,³ Denis Vasiukov,¹ Oskar Stepancic,² Vítor Alexandre de Oliveira Lima,³ Lukas Aniansson,² Paul Steadman,⁴ Manuel Valvidares,⁵ Jörg Schwenke,⁶ Claudiu Bulbucan,⁶ and Elizabeth Blackburn²

¹European Spallation Source ERIC, Partikelgatan 2, 224 84 Lund, Sweden

²Division of Synchrotron Radiation Research, Lund University, 22100 Lund, Sweden

³Jülich Centre for Neutron Science (JCNS-2), Forschungszentrum Jülich GmbH, 52425 Jülich, Germany

⁴Diamond Light Source, Didcot, Oxfordshire, United Kingdom

⁵ALBA Synchrotron, Cerdanyola del Vallès, Barcelona, Spain

⁶MAX IV Laboratory, Lund University, P O Box 118, 22100 Lund, Sweden

We report an experimental investigation of the depth-dependent domain wall formation in L1₀-FePd thin films with high perpendicular magnetic anisotropy. Using circular dichroism X-ray resonant magnetic scattering (CD-XRMS) as a function of the incident X-ray angle, we explore the depth evolution of chiral spin textures in two samples with different strengths of magnetocrystalline anisotropy. Combined with CD-STXM, CD-ptychography, and macroscopic characterization of the structural order, magnetic properties, and surface morphology, we relate these observations to differences in the long-range order of the L1₀ phase of FePd. One FePd thin film with very high magnetocrystalline anisotropy, characterized by $Q_{PMA} = 1.8$, exhibits an unexpectedly large Néel contribution. Angular-dependent CD-XRMS directly reveals a smooth transition from a hybrid Bloch-Néel chirality within the upper FePd layer towards a purely Néel-type structure at the lower FePd interface. In the second FePd sample, despite a still relatively large $Q_{PMA} = 1.45$, the domain walls were found to be purely Néel type. These results indicate a crucial role of the long-range structural order in determining the formation of the magnetic structure.

I. INTRODUCTION

Magnetic domain walls and chiral spin structures in ferromagnetic thin films exhibiting perpendicular magnetic anisotropy (PMA) have attracted considerable attention because of their unique interactions with spin currents and their relevance for modern spintronic technologies, including magnetic recording, logic, and memory devices [1–3]. Devices based on the motion of magnetic domain walls can provide efficient low-power, high-velocity information transport [3, 4]. Recent studies on magnetic thin films hosting spiral magnetic textures discovered a broad range of emergent phenomena, including topological-chiral interactions [5], coupling to materials with strong spin-orbit interaction [6], and interactions with superconductors [7]. These make ferromagnetic thin films with PMA and chiral spin structures highly promising for hybrid heterostructures used in energy-efficient spintronic devices [3].

PMA plays a dual role in such systems. While it stabilizes the out-of-plane magnetization required for perpendicular recording media, it can also suppress interface-driven magnetic textures such as closure domains, which themselves are promising information carriers for next-generation memory and neuromorphic computing concepts [2, 8]. Furthermore, high PMA provides stable, narrow domain walls [9], reduced depinning current densities [3], and enhanced current-driven domain-wall mobilities [4, 10]. Thus, understanding the interconnection between PMA and the domain wall chirality is crucial for an efficient use in spintronic applications. In the present work, we explore the evolution from Bloch- to Néel-type

domain walls and their chirality as a function of depth in FePd thin films with different strength of PMA.

In perpendicularly magnetized systems, cycloidal Néel-type and helicoidal Bloch-type domain walls represent the two fundamental configurations, and are schematically displayed in Fig. 1 (a,d). Their formation is governed by the interplay between perpendicular magnetic anisotropy, dipolar interactions, interfacial effects, and the Dzyaloshinskii-Moriya interaction (DMI) [11]. The magnetic structure of domain walls in thin films with PMA is often considerably more complex than a simple Bloch- or Néel-type configuration. Kittel [12] predicted that domain walls in thin films with PMA may consist of Bloch walls in the film interior with Néel caps forming near the surfaces in order to minimize stray-field energy. This has later been experimentally confirmed in low-PMA FePd [3, 13], as well as in CoCrPt thin films with PMA [3]. Dürr *et al.* [13] demonstrated for low-PMA films the existence of Néel-type closure domains near the surfaces of FePd thin films using circular dichroism X-ray resonant magnetic scattering (CD-XRMS). Navas *et al.* [3] showed by polarized neutron reflectometry that, depending on the film thickness and PMA, such thin films host Bloch-like walls in the center of the film together with Néel caps at the surfaces and intermediate transition regions.

Deviations from a simple picture of Bloch domain walls in the film interior and Néel-type closure domains at the interfaces have been predicted by Legrand *et al.* [14] in dependence of the DMI. However, anisotropic DMI is strongly influenced by both the magnetocrystalline anisotropy and structural defects [11, 15, 16]. In such

systems, in which micromagnetic simulations require the precise knowledge of the underlying crystalline structure, a direct observation of depth-dependent chiral magnetic domain walls is challenging and yet missing.

In this paper, we employ CD-XRMS to investigate the magnetic domain wall structure as function of depth inside two FePd thin films with $L1_0$ structural ordering and different strength of PMA. In particular, we will utilize the results of Chaleau *et al.* [17], who demonstrated that the shape of the circular dichroism pattern in CD-XRMS in reflection geometry can be used to unambiguously identify both the type and chirality of domain walls as schematically shown in Fig. 1. $L1_0$ -ordered FePd thin films exhibit out-of-plane magnetic domains characterized by alternating magnetization perpendicular to the sample surface. This arises from strong uniaxial PMA energy (E_{MA}), a consequence of the symmetry inherent to the $L1_0$ crystal structure [18]. The PMA gives rise to an easy magnetization axis along the $\langle 001 \rangle$ direction, with Bloch-type (helical) domain walls within the film interior, depending on the magnitude of the strength of the magnetocrystalline anisotropy [3, 9]. For magnetic flux closure, this leads to Néel-type (cycloidal) closure domains near the film surfaces. Combining CD-XRMS at constant incident angle, and micromagnetic modelling [19, 20], it has been found that the ratio between shape anisotropy and the PMA governs the ratio between Bloch- vs. Néel-type domain walls in FePd: low PMA leads to large Néel-type closure domains [19], while they have been predicted as not stable under strong PMA.

While Chaleau and Legrand *et al.* [14, 17] have investigated the CD-XRMS pattern at a fixed incident angle and evaluated the depth structure using micromagnetic simulations, here we probe the depth-dependent Bloch and Néel-type domain wall formation experimentally by employing CD-XRMS as function of the incident X-ray angle, and combine our findings with observations from CD-based Scanning Tunneling X-Ray Microscopy (CD-STXM) and CD-Ptychography. We correlate the magnetic domain wall structure with the observed structural properties, influenced by grain boundaries and terrace-like surface features.

The article is structured as follows: Section II describes the sample growth method and details on the employed sample systems, as well as the experimental techniques used for an analysis of the magnetic domain wall structure. Section III outlines the results observed for two FePd thin films. The observations are compared and discussed with respect to their slightly different PMA and related structural quality of the $L1_0$ -phase of FePd. Section IV gives a summary and according outlook towards an inclusion of theoretical approaches based on

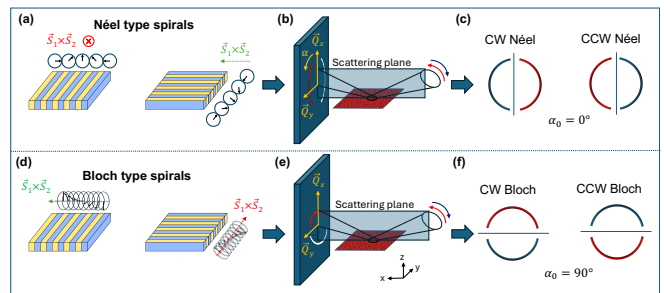


FIG. 1. Schematics of the geometrical considerations for (a-c) Néel-type and (d-f) Bloch type chiral structures [17]: Néel-type chiralities obtain a rotational sense as schematically outlined in (a). Together with the measurement geometry (b), this leads to intensity minima and maxima at $\alpha_{peak} = 90^\circ$, sketched red and blue in (c), respectively, with opposite intensity distributions for clock-wise versus counter-clockwise Néel chiralities. Bloch-type chiralities (d) in this measurement geometry (e) lead to minima and maxima at $\alpha_{peak} = 0^\circ$ (f). Chiral structures that can be detected in this geometry are marked green, while chiralities with $\vec{c} \parallel \vec{y}$ cannot be detected in this setup (marked red).

first-principles and micromagnetic simulations.

II. METHODS

A. Sample growth and characterization

1. Growth of FePd thin films

$L1_0$ -ordered FePd thin films with point group symmetry $P4/mmm$ were grown following the protocol described in Ref.[21–23]. Two samples, **FePd-high** and **FePd-mid** with different magnetocrystalline anisotropies, controlled by different FePd growth modes and thicknesses, were prepared using a state-of-the-art molecular beam epitaxy system (DCA Instruments, Finland) operated at ultra-high vacuum of 10^{-10} mbar:

- **FePd-high:** Pd (1.5 nm) / FePd (38 nm) / Pd (47 nm) / Cr (4 nm) / MgO(001)
- **FePd-mid:** Pd (2 nm) / FePd (70 nm) / Pd (70 nm) / Cr (1 nm) / MgO(001).

For both samples a Cr seed layer was first deposited onto commercial MgO(001) substrates (MaTecK GmbH) to inhibit interdiffusion, followed by a thick Pd buffer layer to accommodate lattice mismatch. To promote high structural ordering for the growth of the FePd layer, the Pd/Cr/MgO stack was annealed at 500 K prior to the co-deposition of Fe and Pd.

FePd-mid was grown with two subsequent growth modes to achieve a slightly lower magnetocrystalline anisotropy of the FePd layer, while keeping a high structural long range order of the $L1_0$ -ordered phase

consisting of alternating Fe and Pd monolayers. First a shuttered growth at room-temperature, with alternately opening the Fe and Pd shutters, followed by the above described codeposition of Fe and Pd at elevated temperatures of 500 K [24], both with an FePd thickness of 35 nm. In total, this results in the higher FePd layer thickness of 70 nm. A thin Pd capping layer was deposited on top of the FePd to prevent surface oxidation for both **FePd-high** and **FePd-mid** thin films.

2. X-ray diffraction

The structural quality of grown thin films was verified with X-ray diffraction measurements using a Bruker AXS D8 Advance system. Figure 2(e) shows XRD measurements of the FePd (001) and (002) Bragg peaks with $\theta_2(\text{FePd-high})=49.8^\circ$ and $\theta_2(\text{FePd-mid})=49.25^\circ$. These (002) Bragg peak positions correspond to out-of-plane lattice constants of $c_\perp(\text{FePd-high})=3.66\text{\AA}$, and $c_\perp(\text{FePd-mid})=3.7\text{\AA}$, respectively. Considering that L1₀-ordered FePd with the tetragonally distorted structure P4/mmm has a smaller out-of-plane lattice constant compared to disordered FePd (fcc-phase) [21, 25], see table I, which indicates different structural qualities and long-range orders of the L1₀-phase of both samples. The measured values are listed together with comparisons from [21, 25] in table I.

The long-range structural order S of the L1₀-phase has an influence on the ratio between the (001) and (002)-peak structure factors [21, 26], which are proportional to the integrated intensities below the Bragg peaks, $A_{(001)}/A_{(002)}$. A perfect L1₀-phase yields $S = 1$ with finite (001) Bragg peak appearance, while lower structural order is connected to $S < 1$ and lower (001) Bragg intensities, e.g. due to mixed fcc and L1₀-phases, atomic intermixing, or structural defects, and depends strongly on the growth conditions. Here, the samples show a structural order of $S(\text{FePd-high}) = 0.63 \pm 0.02$ and $S(\text{FePd-mid}) = 0.31 \pm 0.04$. In comparison, in [22] a value of $S = 0.8$ was reported for high quality L1₀-phase leading to strong PMA.

3. Magnetization measurements

TABLE I. Magnetic and structural parameters of **FePd-high** and **FePd-mid**.

	K_u (M $\frac{\text{erg}}{\text{cm}^3}$)	Q_{PMA}	D (nm)	S	c_\perp
FePd-high	14.43 ± 0.05	1.8 ± 0.05	70 ± 2	0.63 ± 0.02	3.66\AA
FePd-mid	12.77 ± 0.05	1.45 ± 0.03	58 ± 2	0.31 ± 0.04	3.7\AA
L1 ₀ -FePd[21]	10.3	1.55	≈ 60	0.79	3.714\AA [25]
disordered[21]	0.7	0.11	—	0	3.807\AA [25]
FePd					

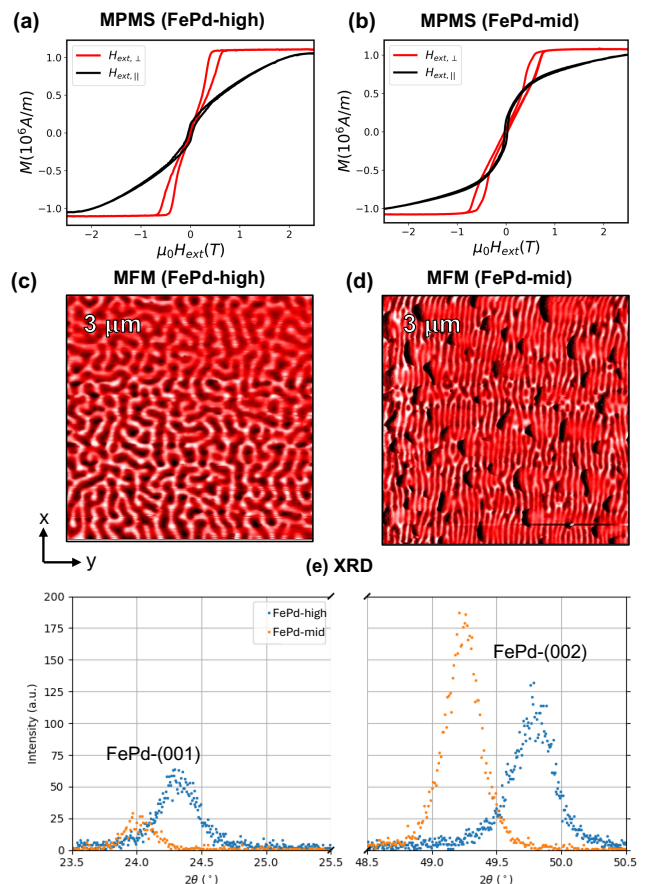


FIG. 2. Magnetic and structural characteristics of samples **FePd-high** and **FePd-mid**: (a,b) Magnetization measurements using an MPMS system (c,d) Lateral magnetic domain pattern as measured by MFM, and (e) XRD measurements of the FePd(001) and FePd(002) Bragg peaks. All measurements are performed at room temperature.

Average bulk magnetization as function of applied magnetic field, $M(H)$, is measured using a magnetic properties measurement system (rf SQUID-MPMS) from Quantum Design at the Juelich Research Center (JCNS-2) in Germany. Figure 1 (a,b) shows the magnetization curves measured at room temperature applied in the directions along ($H_{ext,\parallel}$) and perpendicular ($H_{ext,\perp}$) to the thin film surface. By the ratio of integrated $M(H_{ext,\perp})$ and $M(H_{ext,\parallel})$ hysteresis loops, the magnetocrystalline anisotropy constant K_u can be extracted following equation 1, based on [22]:

$$\int_0^{M_s} (H_{ext,\perp} - H_{ext,\parallel}) dM = K_u + K_{sh}, \quad (1)$$

with the shape anisotropy $K_{sh} = -\frac{1}{2}\mu_0 M_s^2$, and the saturation magnetization M_s . The ratio $\frac{K_u}{K_{sh}}$ yields the quality factor Q_{PMA} , and describes the relative strength of PMA compared to shape anisotropy. High PMA is characterized by values $Q_{PMA} > 1$, whereas

$Q_{PMA} < 1$ indicates higher impact of the shape anisotropy with an in-plane easy magnetization axis, which is described for $L1_0$ -ordered FePd thin films in detail in [24]. The strength of PMA of both samples has been evaluated to $Q_{PMA}(\text{FePd-high}) = 1.8 \pm 0.05$ and $Q_{PMA}(\text{FePd-mid}) = 1.45 \pm 0.03$ for **FePd-high** and **FePd-mid**, respectively.

B. Microscopy measurements

Structural and magnetic surface properties have been investigated at zero magnetic field and at room temperature by Atomic- and Magnetic Force Microscopy (AFM, MFM) using an Agilent 5400 microscope in magnetic ac mode. Figure 2(c,d) shows MFM of **FePd-high** and **FePd-mid** reflecting their conditions during the CD-XRMS measurements: a maze domain structure with interlaced domains in **FePd-high**, while **FePd-mid** exhibits an aligned magnetic domain pattern. The domain width is extracted to $D(\text{FePd-high}) = 70 \pm 2$ nm and $D(\text{FePd-mid}) = 58 \pm 2$ nm by measuring the average peak-to-peak domain distance of the MFM images.

The PMA, magnetic domain width and lateral pattern, as well as the structural order, are interconnected via crystal-field interactions and the spin-orbit coupling [27]: The strength of PMA impacts on the magnetic domain width, which has been evaluated in [21, 22], correlating larger magnetic domain widths with stronger PMA. The lateral domain pattern is maze-like for high PMA, whereas a parallel stripe pattern can only be achieved in samples of lower PMA [19]. The structural quality of FePd impacts on the PMA. This confirms with the higher PMA, higher domain width, and higher structural order of **FePd-high** together with a maze domain pattern, compared to **FePd-mid** with slightly lower PMA, lower domain width, lower structural order, and a laterally parallel stripe pattern.

C. Circular-Dichroism scanning transmission X-ray microscopy and Circular-Dichroism Ptychography

Both, Circular-Dichroism scanning transmission X-ray microscopy (CD-STXM) and CD-Ptychography image the magnetic domain structure (available from the circular-dichroic component) onto the detector after transmission of the X-ray beam through the thin film sample with perpendicular incidence. Results are displayed in Fig. 3(a,b). They are compared with the FePd surface structure measured by AFM in Fig. 3(c). While STXM is a pixel-by-pixel transmission image of the sample, ptychography uses a larger probe and collects diffraction patterns with overlapping positions on the sample. From the set of diffraction patterns, a high-resolution complex-valued real space image of the sample can be calculated using an iterative phase retrieval algorithm [28, 29]. This method is employed at the Softimax

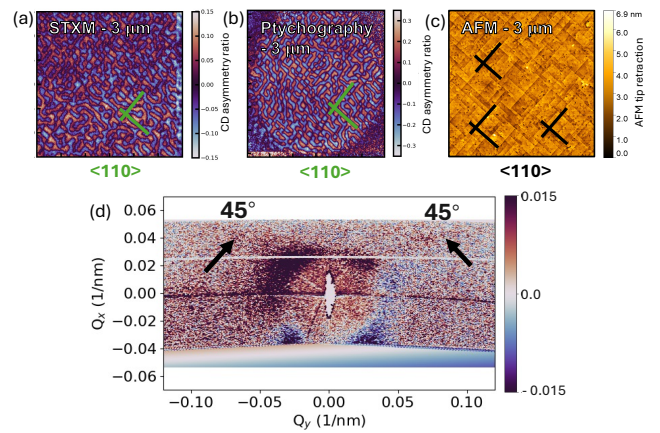


FIG. 3. $3 \times 3 \mu\text{m}$ images of a comparable high-PMA FePd sample, displaying (a) the CD-STXM asymmetry ratio, (b) the CD-Ptychography asymmetry ratio, and (c) the FePd layer surface structure as measured by AFM. (d) shows an exemplary CD-XRMS scattering cross section with artifacts at $\alpha = 45^\circ$ (marked by black arrows), connected to the surface structure. Insets mark the direction of $\langle 110 \rangle$ oriented surface terraces.

Beamline at MAX-IV, Sweden, and yields high-resolution magnetic contrast images of the domain pattern in FePd. We have used an X-ray energy at the Fe L_3 resonance condition ($E = 707$ eV) and have calculated the asymmetry ratio as described in the Appendix A to retrieve the purely magnetic domain pattern.

D. Circular-Dichroism X-ray Resonant Magnetic Scattering

Circular-Dichroism X-ray Resonant Magnetic Scattering (CD-XRMS) measurements of FePd-high and FePd-mid were conducted at two different facilities: the I10 beamline using the endstation RASOR (Diamond Light Source, UK) and at the BL29 beamline using the X-ray scattering endstation MaReS [30] (ALBA Synchrotron, Spain), respectively. Both experiments were performed at room-temperature and zero magnetic field at the Fe L_3 resonance condition ($E = 707$ eV), where the signal becomes specific to iron atoms. Off-resonance scans at $E = 690$ eV (at diamond) and $E = 700$ eV (at ALBA) were also performed for comparison.

At I10, **FePd-high** has been investigated. The sample-to-detector distance was set to $sdd_{I10} = 138$ mm, and the X-ray beam had a size of $200 \times 200 \mu\text{m}^2$. With a sample size of **FePd-high** with $7 \times 10 \text{ mm}^2$, no footprint correction for sample illumination was necessary. To define the magnetic field history, the sample was first saturated out-of-plane in a magnetic field exceeding 1 T, followed by a ramp-down to zero field. Incident angles in the range $\theta_{in} = 10^\circ - 70^\circ$ were used which includes maximum attenuation lengths greater than 60 nm [31]. A

transformation of θ_{in} into the X-ray attenuation length and a comparison with the probed depth of the FePd thin films is performed using the Henke tables [31]. In **FePd-high**, the lower FePd interface to the Pd buffer layer is reached at $\theta_{in} = 40^\circ$.

At BL-29, **FePd-mid** has been investigated. The scattering endstation at BL29 has a sample position with a sample-to-detector distance at $sdd_{BL29}=402$ nm and slit sizes between $5 \times 5 \mu m^2$ - $50 \times 50 \mu m^2$. Here, incident angles of $\theta_{in} = 10^\circ$ - 40° have been investigated. Unfortunately, it was not possible to probe the lower FePd/Pd interface in **FePd-mid** at a thickness above 70 nm.

At both beamlines and at each angle, measurements were carried out using both left- and right-circularly polarized light. By selecting specific polarization channels before and after scattering, different magnetization components can be probed. Magnetic moments lying in the scattering plane, \vec{M}_{\parallel} , are detected in the $\sigma \rightarrow \pi'$ and $\pi \rightarrow \sigma'$ channels, while magnetization components perpendicular to the scattering plane, \vec{M}_{\perp} , are accessed via the $\pi \rightarrow \pi'$ channel [19, 32]. Using circularly polarized light, which couples to the complex magnetic vector $\vec{M}_{\pm} = \vec{M}_{\parallel} \pm i\vec{M}_{\perp}$, allows for probing sinusoidal, helical, or otherwise chiral magnetic structures such as Bloch and Néel walls [19, 33].

For details on the recalculation of the detector image to $I(|Q_x, Q_y|)$, and errorfunction treatment, we refer to the information given in the Appendix A.

E. Identification of Bloch- and Néel-type domain wall chirality from CD-XRMS

Chaleau and Legrand *et al.* [14, 17] demonstrated that a direct experimental observation of the shape of the circular dichroism scattering pattern in CD-XRMS with reflection geometry can be used to determine both the type and chirality of domain walls. Magnetic domains with a scattering vector $|\vec{Q}|$ generate a circular scattering pattern, centered around the specular reflection. Figure 1 displays the typical dichroic scattering pattern for Néel (a-c) and Bloch (d-f) domain walls: A ring-like scattering pattern with $|\vec{Q}|$ corresponding to the periodicity of the domain walls, and an intensity distribution following the extinction rules for a dichroic scattering pattern from chiral magnetic structures along the ring, i.e., following the [34] azimuthal angle α . Néel-structures show a scattering pattern with opposite intensity minima and maxima (sketched red and blue, respectively) on the horizontal, at $\alpha_{peak} = 90^\circ$, and intensity zero-crossings at $\alpha_0 = 0^\circ$. In contrast, helical Bloch walls propagating along \vec{y} produce the opposite pattern, with intensity peaks along the vertical, at $\alpha_{peak} = 0^\circ$ and zero-crossings along the horizontal at $\alpha_0 = 90^\circ$. Clock-wise (CW) and counter-clock-wise (CCW) chiral structures produce

inverted scattering patterns, mirrored at the vertical (Néel) or horizontal (Bloch) lines. A hybrid chiral structure exhibiting a depth-dependent (θ_{in} -dependent) change between Bloch and Néel spirals is characterized by a change of α_0 and the position of peak intensity on $I(\alpha)$. Even for a maze-like domain structure exhibiting a distribution of in-plane oriented domains, the symmetry of the CD-XRMS scattering pattern provides a clear fingerprint for distinguishing between Néel- and Bloch-type spirals oriented along the sample surface.

III. RESULTS AND DISCUSSION

In order to investigate the type and depth-dependence of chiral magnetic domain walls in L1₀-ordered FePd thin films, we performed CD-XRMS measurements as function of incident angle. Figure 4 shows the CD-XRMS measurements collected on **FePd-mid** (a-e) and **FePd-high** (f-j) at selected incident angles between $\theta_{in} = 10 - 30^\circ$, covering a depth-range from 12-32 nm. The radius of the ring-like scattering cross-section $I(|Q|, \alpha)$ defines the domain and domain-wall periodicity. From the scattering ring, $|\vec{Q}|$ is determined as $|\vec{Q}| = (0.042 - 0.05 \text{ nm}^{-1}) \pm 0.003 \text{ nm}^{-1}$, varying slightly as function of depth inside FePd. It arises from the magnetic domains and domain walls in FePd and matches the domain periodicity of 120-140 nm observed by MFM in Fig. 2(c,d).

The data reduction process from raw images to the extracted 2D $I(Q_x, Q_y)$ and the according 1D $I(\alpha)$ at constant $|Q|$, as well as measurement artifacts and their impact, are in detail described in the Appendix A. The black dashed line indicates the azimuthal orientation of α_0 , the intensity zero-crossing. First the chiral nature, and second its depth-dependence is evaluated from Fig. 4 for both samples according to the peak symmetry and intensity distribution, and as function of θ_{in} :

For **FePd-mid**, the 2D CD-XRMS patterns in Figs. 4(a-e) show a constant vertical mirror symmetry (see black dashed line) and constant $\alpha_0 = 0^\circ$ for each incident angle, with sharp intensity maxima (red signal in Fig. 4(a-e)), and minima (blue signal in Fig. 4(a-e)), at $\alpha_{peak} = \pm 90^\circ$, respectively, and increasing intensity as function of depth. To accurately identify α_{peak} and α_0 , we integrate the intensity on the scattering ring as function of $|Q|$. The resulting 1D $I(\alpha)$ unambiguously identify $\alpha_{peak} = \pm 90^\circ$ and $\alpha_0 = \pm 0^\circ$ for each incident angle, which indicate in-plane Néel-type chiral domain walls with constant chiral direction over the whole probed depth of **FePd-mid**.

For **FePd-high**, the 2D CD-XRMS patterns show a rotation of the mirror symmetry and α_0 as function of incident angle in Figs. 4(f-j), marked by the black dashed lines. Accordingly, α_{peak} rotates as function of the inci-

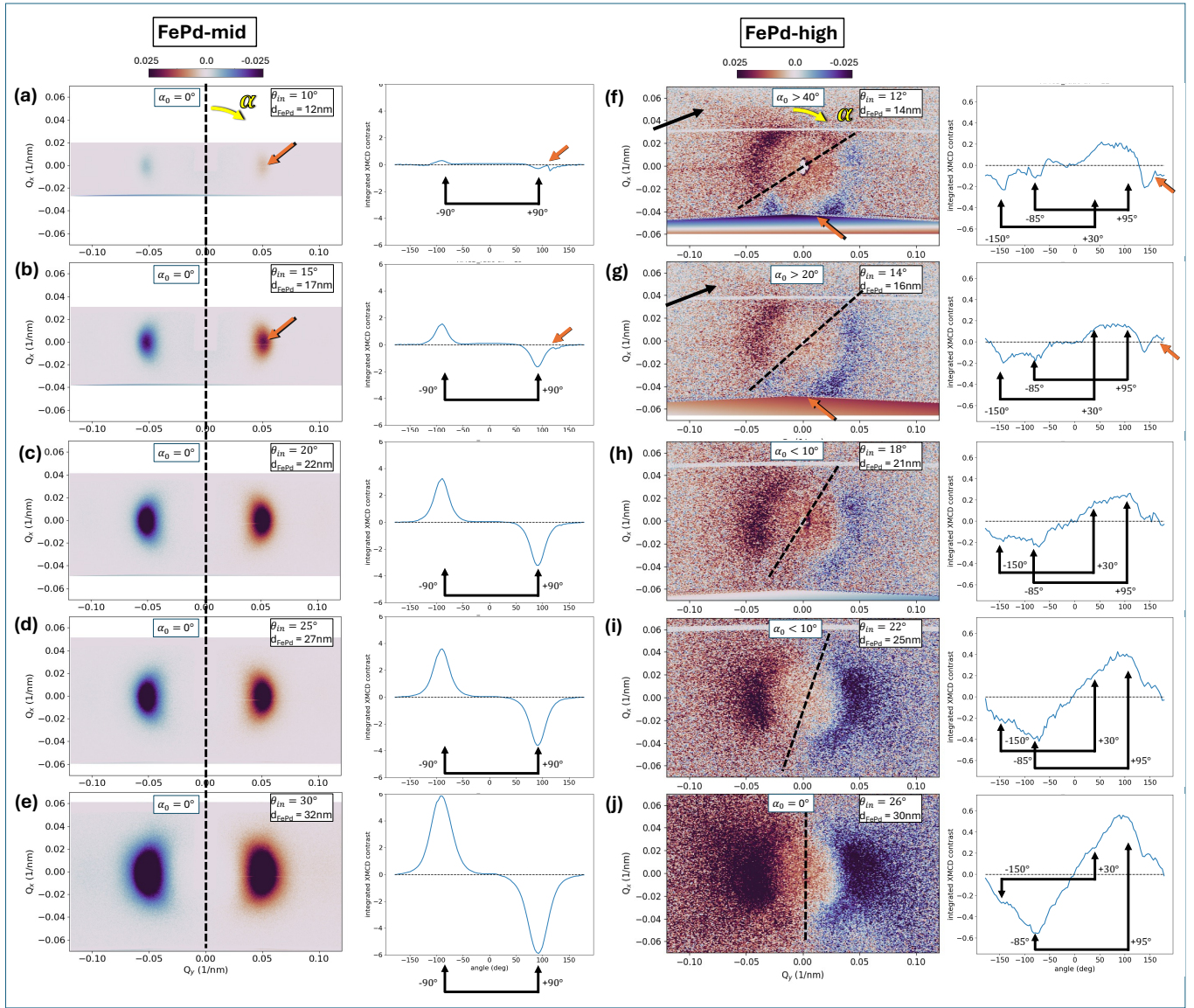


FIG. 4. 2D CD-XRMS patterns (left) and extracted $I(\alpha)$ (right) of (a-e) **FePd-mid** and (f-j) **FePd-high** for selected θ_{in} . The yellow arrow indicates the direction of α , with α_0 marked by a dashed black line. Orange arrows mark impacts from artifacts onto the lineplots of $I(|Q_x, Q_y|, \alpha)$, and are in detail described in the Appendix A. Black arrows mark high-intensity regions at $\alpha = 45^\circ$ connected to the surface structure of FePd as outlined in the discussion.

dent angle, which is evaluated in the 1D line-plots: two π -shifted peak combinations outlined by black arrows are observed (i) at $(-85^\circ, +95^\circ)$, which increases in intensity as function of depth, and (ii) at $(-150^\circ, +30^\circ)$, which stays constant in intensity as function of depth. For (i), a slight shift from the typical Néel-type response at $\alpha = \pm 90$ indicates truncated Néel-type spirals, e.g. from partial magnetic components out of the propagation plane of the Néel spiral. These features are named "Truncated-Néel" (Tr-Néel) structures. The signature (ii) at $(-150^\circ, +30^\circ)$, indicates the additional existence of a hybrid Bloch-Néel-spiral, as proposed by [14], and corresponding to mirror symmetries in between horizontal and vertical with values of $\alpha_0 > 40^\circ$

close to the FePd layer surface. As a function of incident angle, this tilted mirror symmetry rotates monotonically into a vertical symmetry. Considering that horizontal mirror symmetries denote a Bloch-type chirality, and vertical mirror symmetries denote a Néel-type chirality, this suggests a crossover from a hybrid Bloch-Néel-type spiral to a pure Néel-type spiral, as a function of depth inside the FePd layer.

Figure 5(a) presents the lineplots $I(|Q|, \alpha)$ of **FePd-high** in Fig. 4(a) for selected incident angles to superimpose the trend as function of incident angle. Corresponding to a hybrid Bloch-Néel-spiral, an according shift of the zero-peak position α_0 is expected. A

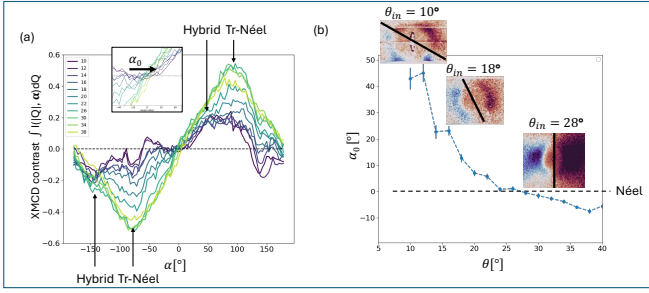


FIG. 5. (a) $I(|Q_x, Q_y|, \alpha)$ of **FePd-high** for selected θ_{in} , arrows mark the positions of Néel- and Bloch-type contributions, and the inset indicates a shift of α_0 with θ_{in} . (b) Sinusoidal fit results of α_0 to (a) as function of θ_{in} . Additional insets visualize the rotation of α_0 in the 2D scattering images with increasing θ_{in} .

sinusoidal fit to each $I(|Q|, \alpha)$ was used to estimate α_0 , with results of α_0 shown in Fig. 5(b). A systematic shift from $\alpha_0 = -40^\circ$ to $\alpha_0 = 0^\circ$ with increasing θ_{in} is observed, as highlighted in the inset in Fig. 5(a). Comparison with the two-dimensional scattering patterns (see insets in Fig. 5(b)) confirms a rotation of α_0 . Altogether, this supports the existence of a hybrid Bloch-Néel-type spiral at low θ_{in} near the upper FePd layer surface, transitioning to pure Néel walls towards greater depth, i.e., near the FePd/Pd-buffer interface. Surprisingly, both samples exhibiting high PMA with $K_u > 12M \frac{erg}{cm^3}$ show strong contributions from Néel-type closure domains.

In addition to the scattering ring at $|\vec{Q}| = (0.042 - 0.05 \text{ nm}^{-1}) \pm 0.003 \text{ nm}^{-1}$, pronounced scattering intensity of the CD-XRMS patterns in Fig. 4 at $\alpha = 45^\circ$ has been observed, outlined by black arrows in Fig. 3(d)). This can be observed in all measurements on **FePd-high**, in both resonant and off-resonant ($E_{off} = 690 \text{ eV}$) conditions. The persistence of this feature off resonance indicates a structural origin. To evaluate their origin, CD-STXM and CD-Ptychography of a similar sample to **FePd-high** with high PMA have been performed to obtain an image of the magnetic domain structure on the basis of circular dichroic X-rays. A preferred lateral direction of magnetic domains along the $\langle 110 \rangle$ crystalline directions can be observed, marked by green lines in Fig. 3(a,b)). A comparison with AFM in Fig. 3(c) shows the same directional ordering of a surface terrace structure, marked by orange lines. Typically, in high-PMA FePd with long-range structural order, grain boundaries can lead to the observed surface terraces and are a sign of high-quality epitaxial L1₀-ordered FePd [35], such as **FePd-high**.

IV. CONCLUSION

We compare the depth-dependent coexistence of chiral Néel and Bloch domain walls of two high-PMA FePd thin films exhibiting slightly different magnetocrystalline anisotropy and Q_{PMA} -values: **FePd-high** with $Q_{PMA}(\text{FePd-high}) = 1.8 \pm 0.05$, and **FePd-mid** with $Q_{PMA}(\text{FePd-mid}) = 1.45 \pm 0.03$. The lower Q_{PMA} of **FePd-mid** is expected to be associated with larger Néel closure domains compared to **FePd-high** [19]. This manifests in a virgin-state magnetic stripe domain pattern, as opposed to the maze domain structure observed in the higher-PMA sample. Still, with its strong out-of-plane anisotropy and $Q_{PMA} > 1$, it is expected to obtain a strong impact from Bloch domain walls. However, we observed that **FePd-high** ($Q_{PMA}(\text{FePd-high}) = 1.8 \pm 0.05$) exhibits a hybrid Bloch-Néel spiral with overlapping chiral components, while **FePd-mid** ($Q_{PMA}(\text{FePd-mid}) = 1.45 \pm 0.03$), although of nominally high-PMA, supports pure Néel-type chiral domains. The slightly higher PMA of **FePd-high** reflects in the typical maze domain structure, and higher structural quality, leading to the formation of surface terraces and the alignment of magnetic domains along these. Both **FePd-high** with $K_{u, FePd-high} = 14.43 \pm 0.05 \text{ Merg/cm}^3$ and **FePd-mid** with $K_{u, FePd-mid} = 12.77 \pm 0.05 \text{ Merg/cm}^3$ obtain larger magnetocrystalline anisotropy constants than reported for a similar, magnetically maze domain structured CoCrPt thin film with $K_u = 1.225 \text{ Merg/cm}^3$ within a 20 nm thin film [3], in which an overall contribution of 25% from pure Néel-type caps for flux closure at the thin film surfaces has been reported.

Regarding the depth dependence of the magnetic structure, the crossover from a hybrid Bloch-Néel spiral to a purely Néel-type spiral occurs at $\theta_{in} = 24^\circ$, corresponding to a probing depth of approximately 25 nm [31]. Overall, the **FePd-high** sample has a total thickness of 38 nm, consisting of approximately 25 nm of hybrid Bloch-Néel spirals and 13 nm of purely Néel-type spirals located near the lower FePd/Pd buffer interface, corresponding to 34% of the total sample thickness. Sample **FePd-mid** exhibits purely Néel-type spirals over the whole FePd layer thickness, even for relatively large $Q_{PMA} = 1.45$.

The origin of the preferred handedness of observed Bloch-type domain walls is referred to an existence of DMI with preferential direction driven by structural defects with a preferred orientation, interdiffusion, or grain boundaries, as discussed in [16]. An in-plane preferential direction of the magnetic domains along the $\langle 110 \rangle$ directions is observed by STXM and Ptychography in Fig. 3. This corresponds to the orientation of surface terraces as observed by AFM in Fig. 3(c), which originate from grain boundary growth along $\langle 111 \rangle$ [35]. Such a preferential orientation can additionally influence the preferred handedness of Néel and Bloch spirals with in-

plane propagation. In addition, direct contact between FePd and the underlying Pd buffer layer can induce non-negligible spin-orbit interactions that distort spin spirals.

The presented results highlight the importance of detailed structural and depth-sensitive magnetic studies, as differences in the domain wall configurations can arise even in nominally similar systems. The observed behavior suggests that subtle changes in microstructure or interfacial effects, such as induced DMI, play a decisive role in stabilizing different chiral spin textures. Our findings challenge the conventional expectation that systems with strong PMA predominantly host Bloch-type spin spirals without preferred handedness and only surface-near contributions from Néel closure domains. This strongly impacts their application in spintronic devices, in which a tuning of the chiral magnetic states requires detailed knowledge about both the lateral and depth-dependent magnetic structure.

These experimental insights form a solid basis for future theoretical investigations for a quantitative analysis of the domain wall contributions, using first-principles calculations and micromagnetic simulations, which are needed to disentangle the interplay between competing energy contributions (magnetocrystalline anisotropy, shape anisotropy, and DMI) in determining the magnetic ground state. A better understanding of these mechanisms will not only advance fundamental knowledge, but also inform the design of novel spintronic devices based on engineered chiral domain wall configurations in thin film heterostructures. Future work will aim to directly correlate CD-XRMS measurements and domain wall chirality with DMI effects introduced by structural imperfections, complemented by first-principles calculations and micromagnetic simulations. The insertion of a non-magnetic interlayer between FePd and Pd would help to confirm or rule out artifacts caused by the Pd buffer layer.

V. ACKNOWLEDGEMENTS

The authors would like to thank Diamond Light Source for beamtime, and the staff of beamline I10 for measurements under two proposal rounds: 31510-1, and 35196-1. These experiments were performed at the BOREAS beamline at ALBA Synchrotron with the collaboration of ALBA staff under the Proposal No 2022025733.

We acknowledge MAX-IV for time at the Softimex beamline under Proposal No 20230624

M.V. acknowledges research grants PID2020-116181RB-C32 and PID2023-146354NB-C43 funded by MCIN/AEI/10.13039/501100011033/.

E.K. acknowledges the funding received from the European Union’s Horizon 2020 research and innovation programme under the Marie Skłodowska-Curie grant agreement No 101069104 — PRESSMAG — HORIZON-

MSCA-2021-PF-01.

Appendix A: Data-processing

Data processing was performed as follows: for each incident angle, multiple snapshots were acquired and normalized by their respective counting times. The normalized snapshots were then averaged to generate a two-dimensional image per incident angle. To propagate uncertainties in the averaged dataset, the error for each pixel was calculated using

$$\Delta I = \frac{\sum_N c_{\text{norm}}(\theta)}{(N-1)N},$$

where c_{norm} is the pixel-wise counting-time normalized count rate, and N is the number of snapshots per incident angle θ . To isolate the magnetic scattering contribution from charge scattering, the circular dichroism signal was computed using the asymmetry ratio in the main text named “XMCD contrast”):

$$I = \frac{I_l - I_r}{I_l + I_r},$$

where I_l and I_r denote the intensities for left- and right-circularly polarized light after normalization and summing, respectively. To observe the full symmetry of the scattering pattern, measurements were performed without a beamstop, with reduced counting time per snapshot to avoid saturation of the CCD detector. For ΔI we have used the gaussian error propagation of pixel-wise error values originating from I_l and I_r .

The subsequent data analysis steps for each incident angle are outlined in Fig. 6. Step 1: detector pixel coordinates were converted into reciprocal space vectors Q by applying a projection correction to account for the Ewald sphere curvature on the flat detector, enabling extraction of the full scattering vector components (Q_x, Q_y, Q_z) . Step 2: Each image was then transformed into the representation $I(|Q|, \alpha)$, where α is the azimuthal angle around the specular peak. Step 3: This transformation was used to analyze the symmetry of the scattering pattern by integrating over a given range in $|Q|$, $\int(I(|Q|, \alpha)d|Q|)$, which yields $I(\alpha)$ as 1D lineplot. Step 3 is illustrated according to the reciprocal-space integration picture by the inset within the lineplots, showing the rotation of the zero-angle α_0 . α_0 was extracted from the lineplots by fitting a sinusoidal function to the integrated data $I(\alpha)$.

For **FePd-mid** and **FePd-high**, the integration was done over the ranges $d|Q|(\text{FePd-mid}) = [0.025, 0.075]$ and $d|Q|(\text{FePd-high}) = [0.026, 0.06]$, respectively. For **FePd-high**, the scattering pattern at low incident angles interferes with the beam stop (white line in the images). This possibly leads to the striped zero-intensity-area of $I(Q_x, Q_y)$. Further artifacts are marked by orange arrows: In FePd-high the limited detector coverage (zero

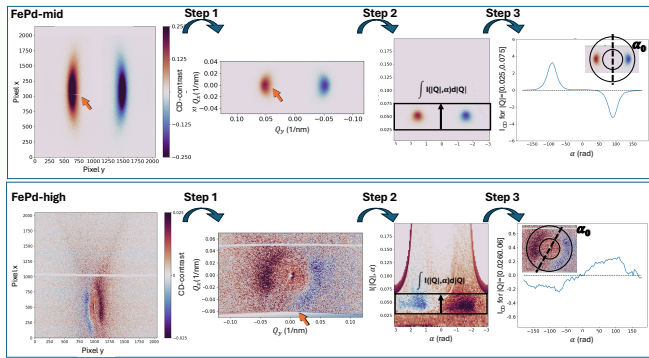


FIG. 6. Data analysis steps (from left to right): (i)

intensity at lower Q_x) impacts on $I(\alpha)$ at $\alpha > 150^\circ$ (artifacts from these regions are largely avoided by limiting the upper Q -value in the integration), and in FePd-mid a sharp line of zero-intensity at $\alpha = 90^\circ$. Measurements of **FePd-mid** were performed without a beamstop. It is important to note that the measured scattering intensity contains information from the sum of penetrated depths: at low θ_{in} , mainly the thin film surface is probed, whereas at higher θ_{in} , both the surface and bulk contribute to the observed scattering pattern. It has to be noted that minor variations of $|\vec{Q}|$ as a function of depth within the FePd layers are observed.

* Corresponding author: annika.stellhorn@ess.eu

- [1] M. Foerster, O. Boule, S. Esefelder, R. Mattheis, and M. Kläui, Domain wall memory device, in *Handbook of Spintronics*, edited by Y. Xu, D. D. Awschalom, and J. Nitta (Springer Netherlands, Dordrecht, 2016) pp. 1387–1441.
- [2] S.-H. Yang, Applied Physics Letters **116**, 120502 (2020).
- [3] D. Navas, C. Redondo, G. A. Badini Confalonieri, F. Batallan, A. Devishvili, O. Iglesias-Freire, A. Asenjo, C. A. Ross, and B. P. Toperverg, Phys. Rev. B **90**, 054425 (2014).
- [4] S. Emori, U. Bauer, S.-M. Ahn, E. Martinez, and G. S. D. Beach, Nature Mater **12**, 611 (2013).
- [5] S. Grytsiuk, J. P. Hanke, M. Hoffmann, J. Bouaziz, O. Gomonay, G. Bihlmayer, S. Lounis, Y. Mokrousov, and S. Blügel, Nature Communications **11**, 511 (2020).
- [6] E. Skoropata, J. Nichols, J. M. Ok, R. V. Chopdekar, E. S. Choi, A. Rastogi, C. Sohn, X. Gao, S. Yoon, T. Farmer, R. D. Desautels, Y. Choi, D. Haskel, J. W. Freeland, S. Okamoto, M. Brahlek, and H. N. Lee, Science Advances **6**, eaaz3902 (2020).
- [7] J. W. A. Robinson, J. D. S. Witt, and M. G. Blamire, Science **329**, 59 (2010).
- [8] W. Jiang, G. Chen, K. Liu, J. Zang, S. G. te Velthuis, and A. Hoffmann, Physics Reports **704**, 1 (2017).
- [9] S. Blundell, *Magnetism in Condensed Matter* (Oxford University Press, 2001).
- [10] A. V. Davydenko, A. G. Kozlov, N. N. Chernousov, A. A. Turpak, A. S. Pashenko, V. A. Antonov, M. V. Rautskii, A. S. Tarasov, A. V. Ognev, C. H. Wan, X. F. Han, and A. S. Samardak, Phys. Rev. B **112**, 224402 (2025).
- [11] A. K. S. Kevin J. A. Franke, Colin Ophus and C. H. Marrows, PHYSICAL REVIEW LETTERS **127**, 10.1103/PhysRevLett.127.127203 (2021).
- [12] C. Kittel, Phys. Rev. **70**, 965 (1946).
- [13] H. A. Dürr, E. Dudzik, S. S. Dhesi, J. B. Goedkoop, G. van der Laan, M. Belakhovsky, C. Mocuta, A. Marty, and Y. Samson, Science **284**, 2166 (1999), [DOI: 10.1126/science.284.5423.2166].
- [14] W. Legrand, J.-Y. Chauleau, D. Maccariello, N. Reyren, S. Collin, K. Bouzehouane, N. Jaouen, V. Cros, and A. Fert, Science Advances **4**, eaat0415 (2018).
- [15] P. C. Carvalho, I. P. Miranda, J. Brandão, A. Bergman, J. C. Cezar, A. B. Klautau, and H. M. Petrilli, Nano Letters **23**, 4854 (2023).
- [16] A. Stellhorn, J. G. C. Palma, A. Backs, A. Bergman, A. B. Klautau, E. Kentzinger, C. Bednarski-Meinke, S. Tober, E. Blackburn, J. Barthel, H. M. Petrilli, and I. P. Miranda, arXiv preprint arXiv:2604.02824 (2026).
- [17] J.-Y. Chauleau, W. Legrand, N. Reyren, D. Maccariello, S. Collin, H. Popescu, K. Bouzehouane, V. Cros, N. Jaouen, and A. Fert, Phys. Rev. Lett. **120**, 037202 (2018).
- [18] D. E. Laughlin, K. Srinivasan, M. Tanase, and L. Wang, Scripta Materialia **53**, 383 (2005).
- [19] G. van der Laan, K. Chesnel, M. Belakhovsky, A. Marty, F. Livet, S. Collins, E. Dudzik, A. Haznar, and J. Attané, Superlattices and Microstructures **34**, 107 (2003).
- [20] E. Dudzik, S. S. Dhesi, H. A. Dürr, S. P. Collins, M. D. Roper, G. van der Laan, K. Chesnel, M. Belakhovsky, A. Marty, and Y. Samson, Phys. Rev. B **62**, 5779 (2000).
- [21] V. Gehanno, *Perpendicular magnetic anisotropy of epitaxial thin films of FePd ordered alloys*, Ph.D. thesis, Université JoSeph-Fourier - Grenoble I (1997).
- [22] V. Gehanno, A. Marty, B. Gilles, and Y. Samson, Physical Review B **55**, 12552 (1997).
- [23] V. Gehanno, R. Hoffmann, Y. Samson, A. Marty, and S. Auffret, Eur. Phys. J. B **10**, 457 (1999).
- [24] A. Stellhorn, A. Sarkar, E. Kentzinger, M. Waschke, P. Schöffmann, S. Schröder, G. Abuladze, Z. Fu, V. Pipich, and T. Brückel, Journal of Magnetism and Magnetic Materials **476**, 483 (2019).
- [25] T. Ichitsubo and K. Tanaka, Journal of Applied Physics **96**, 6220 (2004).
- [26] B. E. Warren, X-ray diffraction (Addison-Wesley Pub. Co., 1969).
- [27] J. M. D. Coey, *Magnetism and Magnetic Materials* (Cambridge University Press, 2010).
- [28] P. Thibault and M. Guizar-Sicairos, New Journal of Physics **14**, 063004 (2012).
- [29] B. Enders and P. Thibault, Proc. A **472** (2196), 20160640 (2016).
- [30] A. Barla, J. Nicolás, D. Cocco, S. M. Valvidares, J. Herrero-Martín, P. Gargiani, J. Moldes, C. Ruget, E. Pellegrin, and S. Ferrer, Journal of Synchrotron Radiation **23**, 1507 (2016).
- [31] E. G. B.L. Henke and J. Davis, Atomic Data and Nuclear Data Tables **54**, 181 (1993).

- [32] J. P. Hill and D. F. McMorrow, *Acta Crystallographica* **A52**, 236 (1996).
- [33] J. P. Hannon, G. T. Trammell, M. Blume, and D. Gibbs, *Phys. Rev. Lett.* **61**, 1245 (1988).
- [34] S. L. Zhang, G. van der Laan, W. W. Wang, A. A. Haghighirad, and T. Hesjedal, *Phys. Rev. Lett.* **120**, 227202 (2018).
- [35] D. Halley, Y. Samson, A. Marty, P. Bayle-Guillemaud, C. Beigné, B. Gilles, and J. E. Mazille, *Phys. Rev. B* **65**, 205408 (2002).